Correspondence to:

J. L. Warner,
james.warner@metoffice.gov.uk

Author Contributions:

Conceptualization: James L. Warner, Callum Munday, Sebastian Engelstaedter
Data curation: James L. Warner
Formal analysis: James L. Warner
Investigation: James L. Warner, Callum Munday, Sebastian Engelstaedter
Methodology: James L. Warner, Callum Munday, Sebastian Engelstaedter
Project administration: James L. Warner
Resources: James L. Warner
Software: James L. Warner
Validation: James L. Warner
Visualization: James L. Warner

Resolving the Turkana Jet—Impact of Model Resolution in Simulating Channel Flow and Inversions

James L. Warner[1] ![ORCID], **Callum Munday[2]** ![ORCID], **and Sebastian Engelstaedter[2]** ![ORCID]

[1]UK Met Office, Exeter, UK, [2]Climate Research Lab, School of Geography and the Environment, University of Oxford, Oxford, UK

Abstract The Turkana Jet plays a pivotal role in the meteorology of East Africa across timescales, and owes its existence to both large-scale dynamics and the representation of intricate local-scale processes. However, much of our understanding of the jet relies on reanalysis, and these along with climate models that produce important projections do not represent these local-scale processes. We systematically investigate the impact of changing model horizontal and vertical resolution in simulating the Turkana Jet, and associated local and large-scale processes. We perform simulations to coincide with the Radiosonde Investigation For the Turkana Jet (RIFTJet) campaign, enabling direct model-sonde comparisons in unprecedented detail. We find that increasing horizontal model resolution significantly increases the strength of the jet throughout the channel by up to 30%, while vertical resolution changes have little impact. Horizontal resolutions finer than 2.2 km produce a nocturnal jet ∼2 m/s stronger than observed but perform better during the day. The elevated inversion, which is strongly tied to the strength of the jet, is much better represented in resolutions as high as 1.1 km, whereas the global model at resolution O(∼10 km) is unable to produce any nocturnal elevated inversion. Predictions of jet strength are improved at higher resolution, indicating an important role of local process given that models inherit the same large-scale state. Despite further improvements at resolutions finer than 4.4 km, we recommend that 4.4 km is the minimum horizontal resolution required to capture realistic interactions between these processes. Underestimation of the Turkana Jet could cause considerable errors in moisture advection into Africa.

Plain Language Summary The Turkana Jet plays an important role in the meteorology of East Africa across timescales, and owes its existence to both large-scale patterns in the atmosphere as well as local factors, such as the representation of orography. However, much of our understanding of the jet relies on models with very coarse grid spacing, and climate models that produce important projections in this area are unable to represent these local processes. We systematically investigate the impact of changing model horizontal and vertical resolution in simulating the Turkana Jet and related processes. We perform simulations to coincide with the Radiosonde Investigation for the Turkana Jet (RIFTJet) campaign; enabling direct comparisons to be made with sonde releases in unprecedented detail. We find that experiments with a finer model grid significantly increase the strength of the jet throughout the channel, while changes to the number of vertical levels have little impact. The warmer air that resides around the height of the jet at night, which is strongly tied to the strength of the jet, is much better represented in resolutions as high as 1.1 km, whereas the global model at resolution O (∼10 km) is unable to produce this elevated warm layer.

1. Introduction

The Turkana Jet is a low-level jet that forms between the Kenyan and Ethiopian Highlands, and plays a crucial role in the meteorology of East Africa on diurnal to decadal timescales (King et al., 2021; Kinuthia & Asnani, 1982; Munday, Savage, et al., 2023). Rainfall patterns across East Africa are highly heterogeneous in space and time (Nicholson, 2017), and this is in part due to the Turkana Jet and how it modulates regional low-level divergence (Nicholson, 2016; Vizy & Cook, 2019). The strength of the jet strongly modulates moisture advection from the Indian Ocean into the interior of central and eastern Africa (Munday, Savage, et al., 2023; Munday et al., 2021). This moisture is important in the formation and development of African easterly waves to the west of the Ethiopian Highlands (Hamilton et al., 2020), which propagate along the African easterly jet (Mathon et al., 2002). Therefore, the representation of the Turkana Jet and its impact on regional moisture budgets could feasibly impact more widely on tropical African meteorology within model simulations.

Writing – original draft: James L. Warner
Writing – review & editing: James L. Warner, Callum Munday, Sebastian Engelstaedter

The Turkana Jet tends to occur around 300–400 m above the surface, typically reaching speeds of 14–18 ms^{-1} during April. It owes its existence to a variety of large-scale processes (Munday, Engelstaedter, et al., 2023). These include prevailing wind off the Indian Ocean, subsidence through the Walker circulation, and thermal forcing (Hartman, 2018; Indeje et al., 2001; Nicholson, 2016; Zhao & Cook, 2021). However, these factors only partly explain jet variability; local-scale processes strongly determine the strength and diurnal cycle of the jet. These include orographic channeling (Indeje et al., 2001; Munday, Savage, et al., 2023), and katabatic flow off the surrounding steep terrain (Hartman, 2018; Vizy & Cook, 2019). For other low-level jets, surface nocturnal temperature inversions play an important role in accelerating winds by decoupling the surface from the overlying atmosphere (e.g., Blackadar, 1957). In the case of the Turkana Jet, however, Munday, Engelstaedter, et al. (2023) find that surface-based inversions are weak (<0.3 K) and form infrequently relative to the frequency of jet formation (>90% of nights). Meanwhile, elevated subsidence inversions that form above the jet are stronger (>1 K) and are more persistent. These elevated inversions co-vary diurnally with the height and strength of the Turkana Jet (Munday, Engelstaedter, et al., 2023). Munday, Engelstaedter, et al. (2023) suggest that the elevated inversions may affect jet strength and height by preventing the upward mixing of momentum.

Climate models that provide invaluable projections over central and east Africa typically use model resolutions that are unable to resolve these important processes (Misiani et al., 2020; Oscar et al., 2022). As a result, they may be poorly constrained given the importance of the Turkana channel in determining regional moisture budgets (Munday et al., 2021). More fundamentally, much of our conceptual understanding of the Turkana Jet is based on reanalysis (e.g., ERA-5; Hersbach et al., 2020), which by construction is a parameterized model, with a relatively coarse horizontal grid O($\sim$31 km) that is unable to capture these salient local processes (Munday, Engelstaedter, et al., 2023). More recently, convection-permitting (CP) pan-Africa model simulations at 4.5 km resolution have been performed (Stratton et al., 2018). These simulations provide a first glimpse into understanding the limitations of coarse parameterized models in this complex region (Finney et al., 2019; Misiani et al., 2020; Munday et al., 2021), but no studies have systematically compared the impact of model horizontal and vertical resolution on the Turkana Jet with direct in situ observations. More generally, very few studies evaluate atmospheric dynamics with CP models in conjunction with observations over Africa.

Marsabit is a town located on the northern flank of a basaltic shield volcano at an elevation of 1,337 m, located near the entrance of the Turkana channel (Figure 1a). The Radiosonde Investigation For the Turkana Jet (RIFTJet) observation campaign in March/April 2021 provided an unprecedented view of the Turkana Jet through 3-hourly radiosonde launches at Marsabit (Munday et al., 2022), building on seminal observation campaigns in the 1980s using pilot balloons by Kinuthia (1992). This novel data set provides us with in situ measurements that are urgently needed to assess the fidelity of model simulations in the Turkana channel. Munday, Engelstaedter, et al. (2023) compared sonde data with reanalysis, finding that the latter underestimates the strength of the jet considerably, as well as being unable to capture the elevated inversion above the jet. While the improvement of using high-resolution CP models over parameterized models in simulating the jet is known (Misiani et al., 2020), little is known about the performance of CP models across the turbulence "gray-zone" in this region of complex orography (Kirshbaum, 2020), or in comparison to in situ observations instead of reanalysis data. Furthermore, to the authors knowledge, no studies have documented the impact of model vertical resolution on the jet, despite the possible impact of vertical resolution on simulating the fine-scale nocturnal inversion structures that may be related to the jet. The representation of the elevated inversions may also depend on the strength of wider subsidence in the region, subsequently modulating the jet (Indeje et al., 2001). We seek to investigate the following questions;

- What is the impact of model horizontal and vertical resolution on the nocturnal structure and strength of cross channel flow?
- Does increased model resolution improve the representation of the elevated inversion and jet relative to sonde releases?
- How similar is the large-scale pressure gradient across the channel in the simulations, and thus the relative contribution of local and large-scale processes?
- Is the strength of the inversion linked to the jet, and how skillful are the models in predicting jet strength during the night?

Our results will address the pressing question of what model resolution is required to suitably simulate the Turkana Jet and related processes that are linked to its strength. This will help inform future modeling strategies that span both weather and climate timescales in this important region for African meteorology. This study will
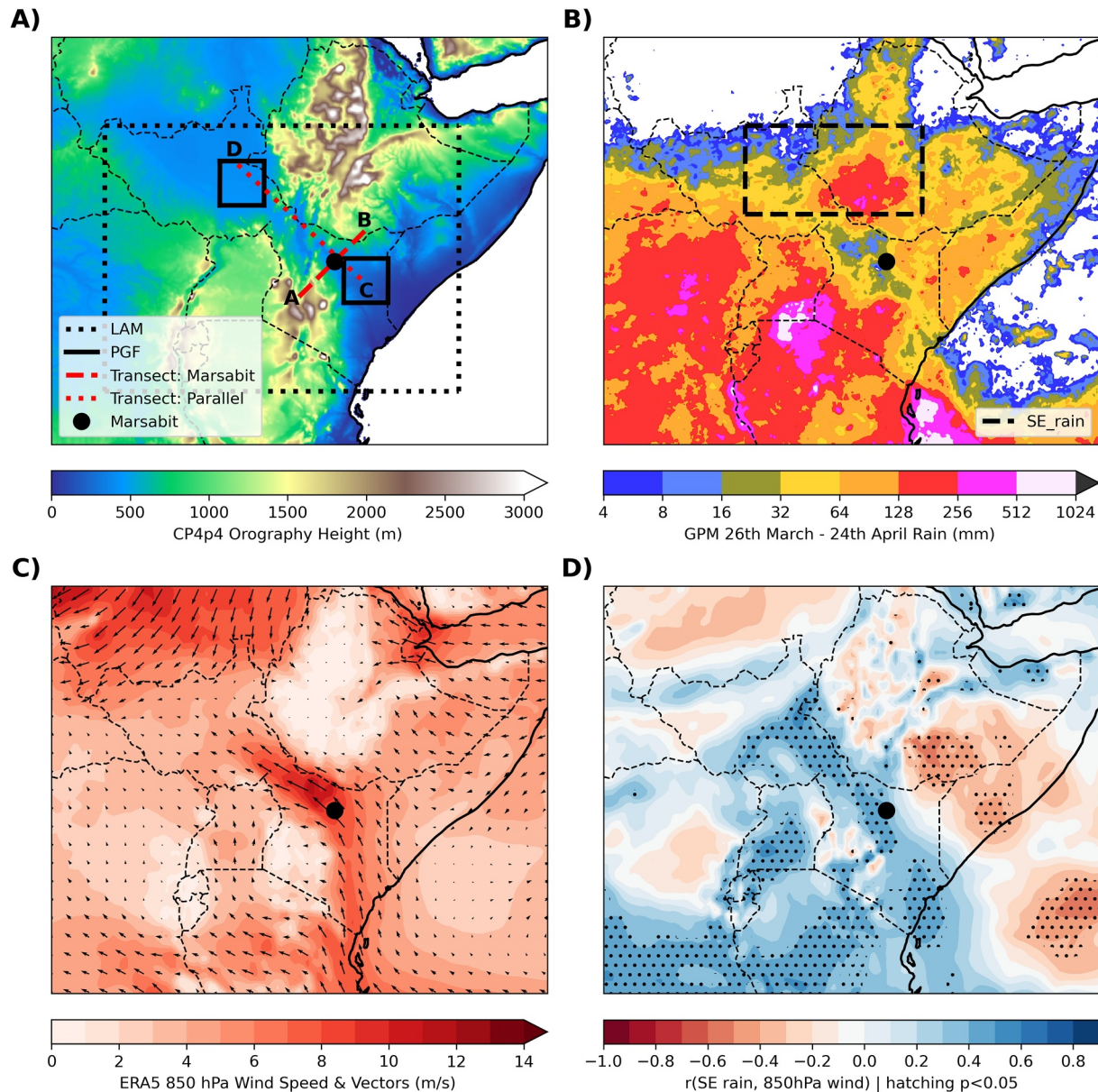
Figure 1. Model setup and climatology over East Africa. (a) Orography height in the 4.4 km operational tropical Africa model is shaded, with the model domain outlined in the dotted black line. The two red lines indicate transects that are used in subsequent analysis. The black squares indicate the regions where the pressure gradient is calculated. The location of Marsabit is denoted by a black circle. (b) GPM rainfall accumulation over the trial, with a bounding box over South Ethiopia used in panel (d). (c) 850 hPa winds using ERA5 hourly reanalysis, averaged over the trial. (d) Instantaneous correlation of daily rainfall in the South Ethiopia bounding box in (b), and daily average 850 hPa wind speed over the trial.

develop both our understanding of missing processes in models within large inter-model consortiums (e.g., Coupled Model Intercomparison Project; Almazroui et al., 2020), as well as numerical weather prediction orientated application which may be of use to rapidly developing renewable industries operating in wind and hydro power through the Turkana channel (Bloomfield et al., 2022; Giuliani et al., 2022; Hafner et al., 2018). Additionally, the results here are likely to be useful for understanding other low-level jets, both in Africa such as the Limpopo Jet and Zambezi Jets (Munday et al., 2021; Spavins-Hicks et al., 2021), and elsewhere over the Great Plains, USA, South America, and Asia (Acosta & Huber, 2017; Helfand & Schubert, 1995; Montini et al., 2019).

The paper is structured as follows; first we describe the model simulations performed and verification data in methods, then we explore each question sequentially in the results section. We conclude the paper by presenting a summary of findings and key recommendations.

Table 1
Overview of the Different Model Configurations Used in This Study

Model experiment name	Horizontal resolution (lat × lon)	Vertical levelset	Horizontal grid (lat × lon)	Science configuration	Timestep (s)
GLM	~0.09 × 0.14 (n1280)	70 Levels 80 km Lid	1,920 × 2,560	GA7.1/GL8.1	240
CP8p8	0.08 × 0.08	80 Levels 38.5 km Lid	188 × 250	RAL2-T	120
CP4p4	0.04 × 0.04	80 Levels 38.5 km Lid	375 × 500	RAL2-T	90
CP2p2	0.02 × 0.02	80 Levels 38.5 km Lid	750 × 1,000	RAL2-T	60
CP1p1	0.01 × 0.01	80 Levels 38.5 km Lid	1,500 × 2,000	RAL2-T	30
CPL70	0.04 × 0.04	70 Levels 80 km Lid	375 × 500	RAL2-T	60

2. Methods

To determine the impact of model resolution on the Turkana Jet, we use the Met Office Unified Model (UM) coupled with the Joint UK Land Environment Simulator to represent the land surface (Best et al., 2011; Cullen, 1993). We use the operational global model (GLM) configuration of the UM at the time of the trial period, which includes the GA7.1/GL8.1 science settings (Walters et al., 2019), at n1280 resolution (~0.14°E/W, 0.09°N/S). While we directly evaluate the GLM forecasts, they are also used to drive a regional limited area model over the Turkana region (outlined in Figure 1a), providing lateral boundary conditions every 3 hr. The regional domains do not contain regional data assimilation and are initialized by directly interpolating the global analysis onto the regional grid. The regional model simulations use the RAL2-T science configuration (Bush et al., 2023), which uses Wilson-Ballard for the microphysics scheme (Wilson & Ballard, 1999), and the Smith cloud scheme (Smith, 1990). The key difference between the RAL2-T and GA7.1/GL8.1 science configurations is that deep convective parameterization is turned off in RAL2-T. Both regional and global simulations involve no ocean coupling; sea surface and lake temperature are prescribed through the operational sea surface temperature and sea ice analysis system (OSTIA, Donlon et al., 2012). Climatological aerosols are used throughout the model integration in both configurations. We initialize our model runs daily at 06Z, and perform 29 integrations during the 25th March 2021–22nd April 2021 inclusive, out to 54 hr. We chose this initialization time and forecast length to match the current operational Tropical Africa model, which runs at 06 and 18Z daily. Initialization at 06Z is chosen as it has a reduced spin-up period compared to 18Z (Warner et al., 2023). When evaluating the diurnal cycle, we use the model $T + 18$ to $T + 42$ hr forecast to allow 18 hr for model spin-up.

To determine the relative impact of model horizontal resolution, which includes the impact of orographic representation, a variety of experiments are performed using grid resolutions from 8.8 to 1.1 km resolution. We also perform an additional experiment to examine the impact of vertical resolution (CPL70), by degrading the number of vertical models in the regional model to match that of the GLM (80–70 levels). A summary of the experiments and their configuration can be found in Table 1. In the regional model configurations used here, model levels follow the terrain surface. In high resolution models, strong gradients in topography can lead to stability errors when grid surfaces are steeply tilted (Shaw, 2018; Sheridan et al., 2023). To counteract this, the standard approach is to use a smoothing technique, by iteratively smoothing the orography at each grid-point based on its adjacent points. More details about this method can be found in Sheridan et al. (2023). Whilst this is applied throughout the model domain to improve stability, work is being done to target this smoothing only where necessary in future UM simulations (e.g., Sheridan et al., 2023). Orography height in these experiments are sourced from the Shuttle Radar Topography Mission (STRM; Farr et al., 2007), and interpolated to the regional grid before smoothing. Orography height for the different model configurations can be found in Figure 2.

The radiosonde launches as part of the RIFTJet campaign were released from the site of the Marsabit meteorology station (WMO identifier 63641), located 37.9735°E, 2.3395°N, at a surface altitude of 1,337 m. Comparison of
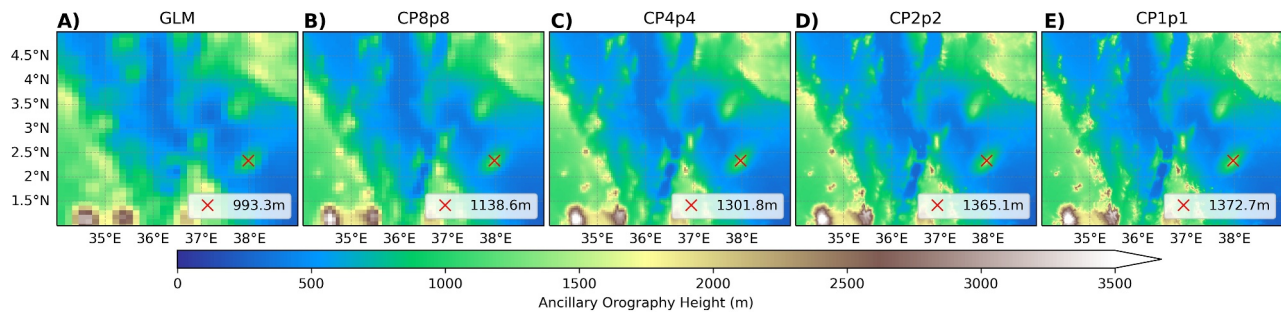
Figure 2. Model orography height across configurations. (a) Model topography height over the Marsabit region in the global model (GLM) experiment. The location of the sonde launches is displayed with a red cross, with the model height shown in the legend using a linear interpolation on the native model grid. Panels (b–e) same as (a), except for CP8p8, CP4p4, CP2p2, CP1p1 respectively.

model data with sondes can be complex, given the drift of the sonde in space in time (e.g., Laroche & Sarrazin, 2013). In this analysis, we are interested in the low-level jet and the elevated inversion, which are typically located in the 30–100 hPa layer above the surface (Munday et al., 2022). Examining the relationship between radiosonde height and time elapsed from launch indicates the typical core of the jet is reached ∼0.1 hr after launch (not shown). We deem this temporal drift in the radiosonde negligible given the processes we are interested in vary over hours. Spatially, the radiosonde consistently drifts westwards and northwards quasi-linearly from 870 hPa (typical surface pressure) through to 750 hPa, above the jet and inversion structure. Ideally, for each launch, we would interpolate the model at the location of the sonde at each pressure level. This is complicated by two different reasons; each model experiment has a different model surface pressure level (due to the representation of orography), and model experiments differ in the number of vertical levels (so any interpolation between model levels might introduce artifacts in the coarser model level-sets). To simplify our comparisons, we take the mean sonde displacement between the surface and 800 hPa (the layer which contains the jet and the inversion), which approximates as 0.02° west/north. We therefore extract model profiles at 37.9535 E, 2.3595 N, using a linear interpolation on the native model grids. We note that this shift is very small, especially compared to some of the model resolutions considered here, and expect it to have little impact on the results presented in this study. We have included some assessment of the jet and related inversions spatially around Marsabit for completeness later in the study.

To produce the overview Figure 1, we use the Global Precipitation Measurement Integrated Multi-Satellite Retrievals (GPM-IMERG) data set (version V06 B, production release; Hou et al., 2014) to determine rainfall over the region during the period. We also use ERA-5 derived 850 hPa wind speed (Hersbach et al., 2020).

3. Results

During the trial period considered here, the Turkana Jet transports moisture-laden air from lower latitudes over the Indian ocean (Figure 1c). Daily rainfall totals over South Sudan and Ethiopia are highly correlated with the mean strength of the Turkana Jet, when using reanalysis in conjunction with GPM-IMERG rainfall (Figure 1d). Lower rainfall than usual fell during the trial period, in part due to the Madden-Julian Oscillation in phases 5 to 8 during the trial (Munday et al., 2022). Notably, lower rainfall totals are found within the Turkana channel compared with the surrounding landscape, especially over Lake Victoria and the highlands (Figure 1b).

3.1. Structure of the Turkana Jet

We first assess the model simulation of the jet across two transects in the channel; one across the entrance of the channel, and one parallel to the channel, both intersecting Marsabit (as shown in Figure 1a). We examine the wind speed, specific humidity, vertical velocity and air temperature averaged across all forecasts during the trial at 00Z (T + 18 hr), when the jet is typically strongest (Munday et al., 2022). At the entrance of the channel, the strength of the jet is positively correlated with increased model resolution (Figures 3a–3f). When considering specific humidity, we find that the higher resolution models also have increased moisture at and below the jet. The combination of increased jet speed and higher water vapor loading indicates around 40% more water vapor is being advected through the entrance of the Turkana channel with higher resolution (8.8 vs. 1.1 km) models. It is
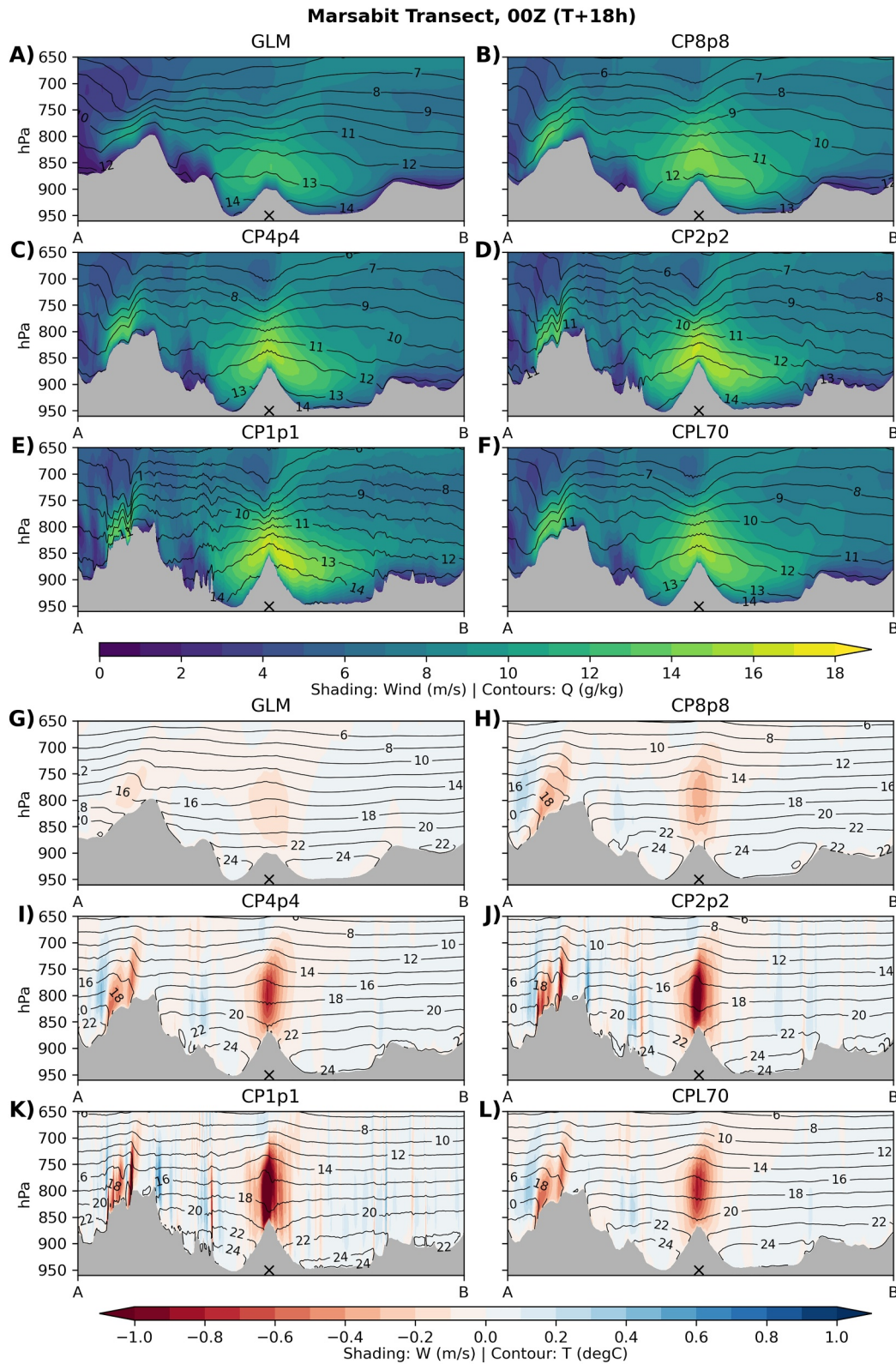
Figure 3.

particularly interesting that there is a further increase of wind speed between 2.2 and 1.1 km model resolution, despite 2.2 km being able to resolve local detail in orography (Figure 2). The GLM, whilst at much higher resolution compared to reanalysis and models that underlie climate projections in this region, produces a broad weak jet. Differences between CP4p4 and CPL70 indicate that the reduced level-set in CPL70 has little impact on the mean jet strength or moisture through this transect.

We next examine vertical velocity and air temperature across the same channel entrance transect (Figures 3g–3l). We find stronger subsidence immediately downstream of Marsabit in the higher resolution simulations, which leads to increased compressional heating. This compressional heating may be related to the elevated inversion that occurs over Marsabit (Munday et al., 2022), and the strength is positively correlated with wind speed. More widely across the channel entrance, the temperature appears uniform across all experiments regardless of horizontal/vertical resolution.

The transect parallel to the channel is shown in Figure 4. Similar to that shown in Figure 3, the jet is stronger throughout the channel as a function of increasing model grid resolution, suggesting higher quantities of moisture advection through the channel into East Africa. While we cannot directly determine whether the increased resolution of orography or increasingly resolved turbulence is behind the jet speed increase, these results show that horizontal resolution has a strong impact on the strength of the Turkana Jet through the channel. Vertical velocities through the channel are largely tied to orography, with broad areas of rising air followed by rapid subsidence downstream of peaks (Figures 4g–4l).

We focus our attention on the area immediately around Marsabit, to determine spatial variability of the jet/inversion within the model simulations. Marsabit is situated on a basaltic volcano and is considerably higher than the surrounding area (Figure 2). We examine the maximum wind speed in the 150 hPa layer above the jet, in order to capture changes in the jet height around orography (as in Figure 4), along with the mean wind direction in the same layer, and present this in the first column of Figure 5. We note that model horizontal resolution not only plays a role in the jet strength locally at Marsabit, but also lee-side with a distinct jet minima. This is correlated with the increased strength of the inversion downstream of Marsabit (Figure 5, second column). Physically, these results would be consistent with the hypothesis of downstream turbulence causing increased frictional heating. The wind vectors indicate that the flow in this layer predominantly rises over Marsabit, and only a small component is diverted around in the higher resolution models.

The elevated inversion, here defined as the difference between maximum temperature in the surface + 20 hPa and surface + 150 hPa layer, and minimum temperature in the surface to surface + 20 hPa layer, shows that the sonde release location is on the boundary of the elevated inversion according to the high-resolution models. We note that all sonde launches follow the mean flow north-west, and so are advected into the inversion as they rise, though the models may be underestimating the magnitude and extent of the elevated inversion. Note that only at resolutions of 4.4 km and lower is the local inversion surrounding Marsabit present. While the vertical level-set appears to have minimal impact on the local inversion, there are large differences downstream with increased vertical resolution producing a stronger inversion (Figures 5j and 5v). The general vertical velocity structure is consistent at resolutions below 8.8 km, there are still subtle differences between the 2.2 and 1.1 km simulations downstream of Marsabit, with evidence of stationary gravity waves (Figure 5s). Finally, we noted that the higher resolution model runs have increased water vapor advected by the jet, despite a similar temperature (Figures 3 and 4). Using a low cloud fraction diagnostic, we note there is considerably more upslope stratus in the higher resolution models (Figure 5t). Low cloud and mist were observed at night during the campaign. This may impact on the surface energy balance upstream of Marsabit and subsequently the representation of the boundary layer and jet structure aloft.

Figure 3. Cross sections across entrance of channel. (a) Winds in all global model (GLM) forecasts are averaged at T + 18 hr (corresponding to 00Z) through the Marsabit transect, as defined in Figure 1, are shaded. The average specific humidity is shown in contours. Regions where the pressure is lower than the average pressure of the lowest model level is shaded in gray. A cross denotes the location of Marsabit along the transect. Panels (b–f) same as (a), except for the CP8p8, CP4p4, CP2p2, CP1p1, and CPL70 experiments respectively. (g) Average GLM vertical velocity through the Marsabit transect, as defined in Figure 1. Air temperature is shown in contours. Panels (h–l) same as (g), except for the CP8p8, CP4p4, CP2p2, CP1p1, and CPL70 experiments respectively.
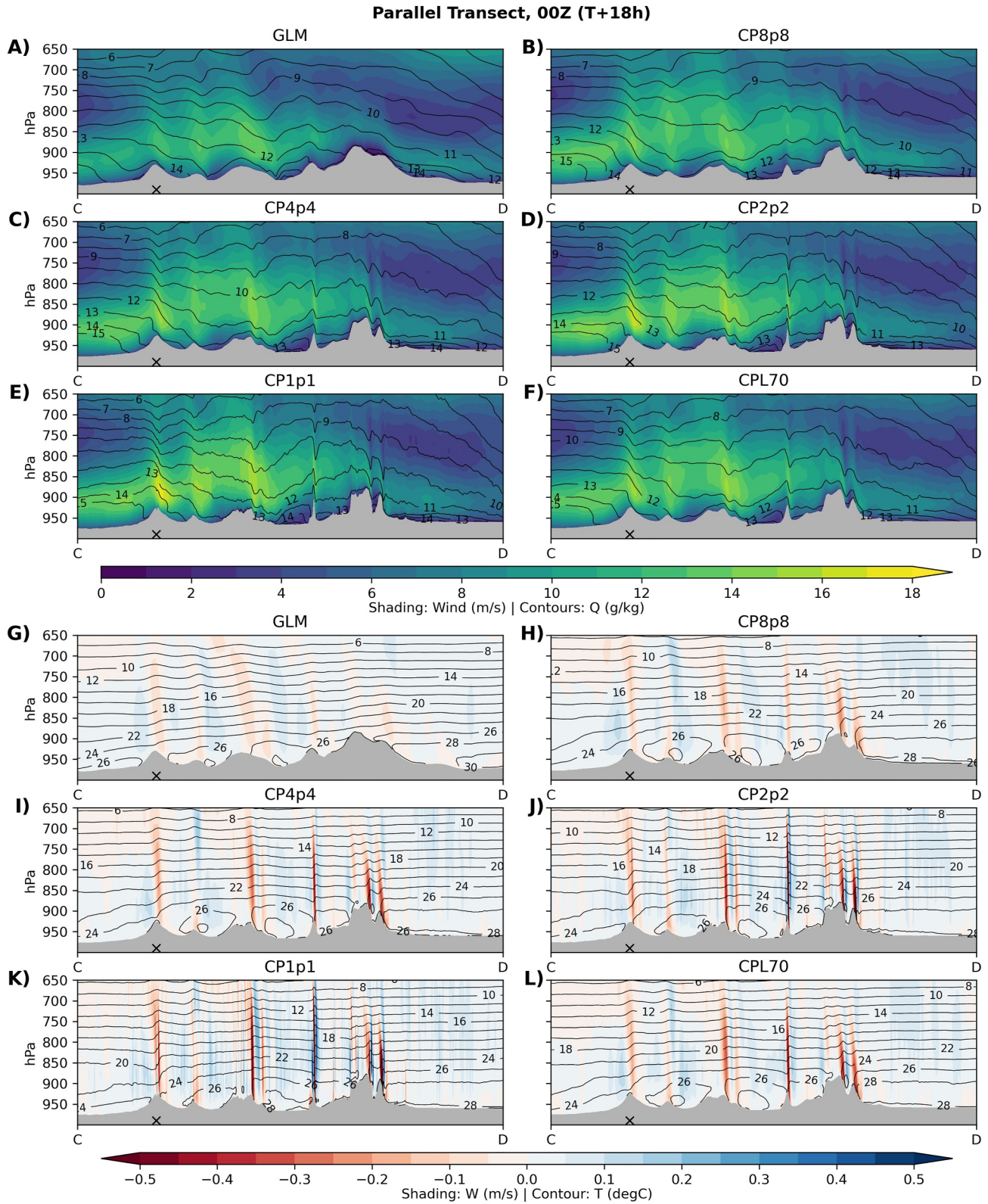
Figure 4.

3.2. Verification Against Radiosonde Data

We next compare our model simulations against the sonde observations at Marsabit from the RIFTJet campaign (Munday et al., 2022), for both wind speed and air temperature (Figures 6 and 7). The sonde wind profiles indicate a narrow jet, confined within the 50 hPa layer above the surface, which peaks in the early hours and persists throughout the day. In all model simulations, the jet extends much higher through the lower atmosphere before it becomes more confined toward the early hours, compared to the radiosonde observations. This may play a role in the model potentially overestimating moisture transport during the late evening through the channel, depending on how representative the radiosonde data is of the broader area (Figure 5). With increasing horizontal resolution, we also note the jet maxima becomes closer to the surface (853 hPa in the 1.1 km simulations, 837 hPa in the 8.8 km simulations). We note that the higher resolution models below 4.4 km horizontal resolution produce a jet that is stronger than seen in the sonde, although the jet speed during the day verifies better for the highest resolution 1.1 km simulation. Above the jet, we also see some differences between the sonde and model simulations. While both models and sonde appear to have a diurnal cycle in winds around 700 hPa, in the models this is more pronounced and slightly out of phase, particularly at high resolution (Figure 6e). This does improve slightly at even higher resolution (Figure 6f).

For air temperature, the 4.4 and 2.2 km simulations compare well against the sonde observations for the elevated inversion that develops at 00Z, and extends through the night till the following morning (Figure 7). In the higher resolution models that capture the inversion, the elevated inversion tends to extend more widely through the column than found in the sonde. In fact, in the highest resolution model, the elevated layer seems to be deeper despite being a similar strength to the sonde. During the day, higher temperatures are confined to near the surface in the sonde profiles, with a likely super-adiabatic lapse rate close to the surface. Model simulations seem to show a much warmer lower atmosphere during the day, with temperatures dropping more linearly with height. Boundary layer diagnostics such as the turbulence mixing height and boundary layer depth indicate that at higher resolutions, the daytime boundary layer is much smaller; around half the height in the 1.1 km simulations compared to the 8.8 km simulations (not shown). This may be related to a residual elevated inversion layer from the night before.

3.3. Large-Scale Flow

We examine the large-scale pressure gradient across the channel to determine whether the representation of the jet is mediating the large-scale within the model domains. We construct two boxes either side of the channel (Figure 1), and compute average mean sea level pressure in each box across the trial (Figure 8). Both the lower and upper basin follow a similar diurnal cycle; a minima during the afternoon at 13Z (local time 4p.m.), and a maxima around 06Z. These can be explained through thermal forcings, such as heating upstream of the channel. Hartman (2018) argue this is one of the largest drivers of wind through the Turkana channel. Causes of the local pressure minima at 00Z may be a combination of local effects and superimposition of the atmospheric tide (etc. Dieminger et al., 1996). Exploring the difference between the lower and upper basin in Figure 10c reveals a pressure gradient force (PGF) up channel that persists during the day, which is highly correlated with the jet speed (i.e., Figure 6). While models broadly behave similarly, there is a suggestion of slightly increased pressure gradient across the channel at night in the higher resolution models, tied to the stronger jet. Given the instantaneous correlation between basin PGF and jet speed, it is not clear which direction of causality exists. The similarity of the models large-scale pressure gradient across the channel suggests an important role for local processes which may explain the differences in model jet and elevated inversion.

3.4. Link Between Inversions and Jet Strength

So far, we have identified key differences in the representation of both the jet and elevated inversion which depend highly on model resolution. In this section, we condense characteristics of the jet and elevated inversion into key diagnostics and explore the link between these and how this varies across model configuration.

Figure 4. Cross sections through the channel. (a) Winds in all global model (GLM) forecasts are averaged at T + 18 hr (corresponding to 00Z) through the Marsabit transect, as defined in Figure 1, are shaded. The average specific humidity is shown in contours. Regions where the pressure is lower than the average pressure of the lowest model level is shaded in gray. A cross denotes the location of Marsabit along the transect. Panels (b–f) same as (a), except for the CP8p8, CP4p4, CP2p2, CP1p1, and CPL70 experiments respectively. (g) Average GLM vertical velocity through the Parallel transect, as defined in Figure 1. Air temperature is shown in contours. Panels (h–l) same as (g), except for the CP8p8, CP4p4, CP2p2, CP1p1, and CPL70 experiments respectively.
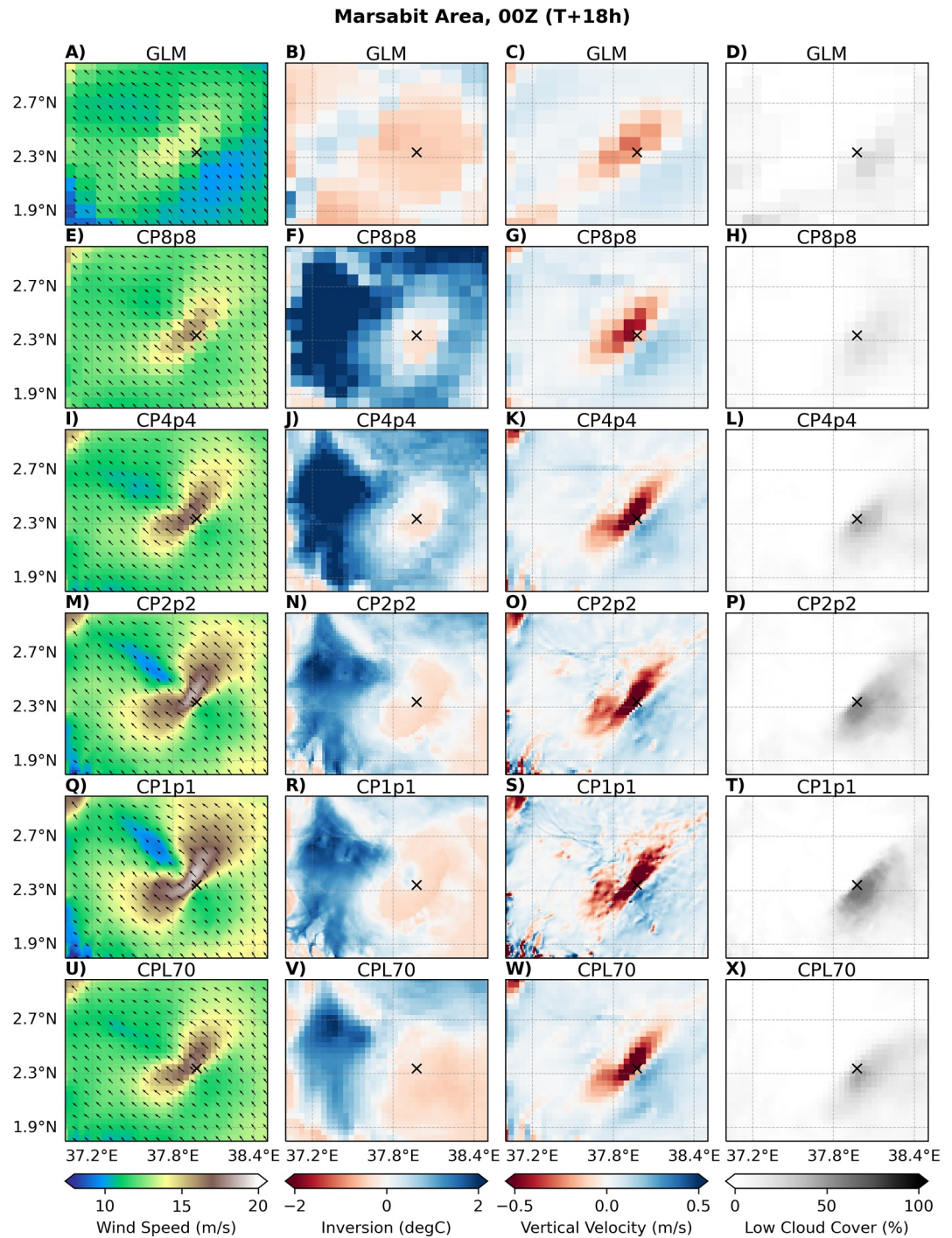
Marsabit Area, 00Z (T+18h)

Figure 5. Spatial variability around Marsabit. (a) Max wind speed, with mean wind direction from the surface to 150 hPa above the surface in the global model (GLM) model at 00Z, averaged across the trial. Wind speed is shown in shading, and the vectors indicate wind direction. (b) The mean inversion strength for the GLM experiment, defined as the difference between the maximum temperature in the surface + 20 hPa and surface + 150 hPa layer, minus the minimum temperature in the surface to surface + 20 hPa layer. This is computed for each 00Z and averaged across the trial. (c) Vertical velocity on the model surface + 50 hPa at 00Z, averaged across the trial for the GLM experiment. (d) Average low cloud fraction at 00Z, averaged across the GLM experiment (e–h) same as (a–d), respectively, for the CP8p8 experiment. Panels (i–l) same as (a–d), respectively, for the CP4p4 experiment. Panels (m–p) same as (a–d), respectively, for the CP2p2 experiment. Panels (q–t) same as (a–d), respectively, for the CP1p1 experiment. Panels (u–x) same as (a–d), respectively, for the CPL70 experiment. In all panels, the location of the sonde launches at Marsabit are shown by a black cross.
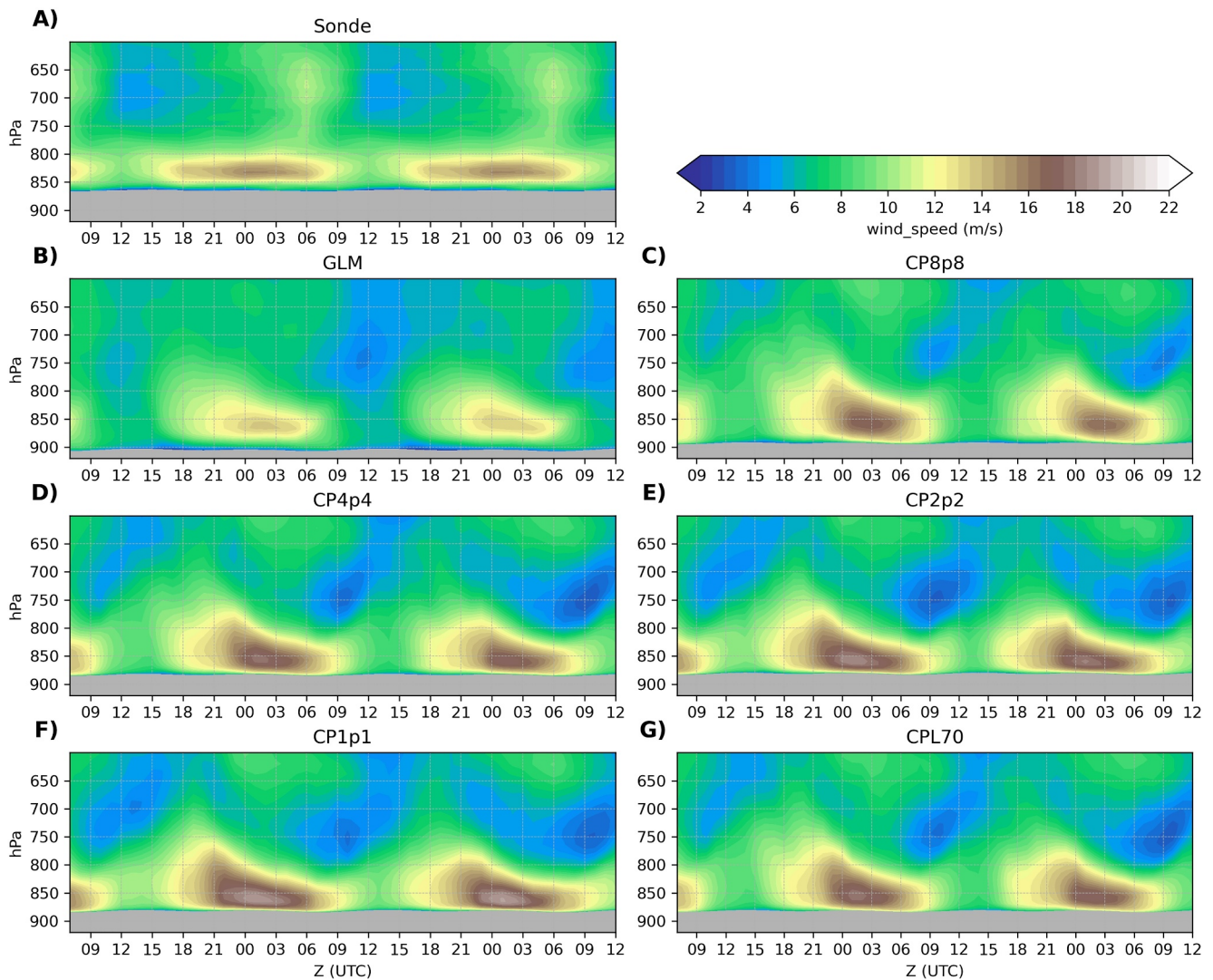
Figure 6. Hovmoeller of wind speed at Marsabit. (a) 3 hourly sonde launches are averaged over the full trial period to produce a hovmoeller of wind speed as a function of time of day. The hovmoeller is shifted and tiled to start at 07UTC, and repeat every 24 hr for subsequent comparison with model data. Pressure levels that fall below the sonde launch pressure are masked in gray. (b) Wind speed in the global model (GLM) experiment as a function of lead time, matching the diurnal cycle (T + 1 hr is 07UTC), averaged across the trial period. Model data is linearly interpolated from the sonde launch site, shifted by 0.02° west and north. Panel (c) same as (b), except for the CP8p8 experiment. Panel (d) same as (b), except for the CP4p4 experiment. Panel (e) same as (b), except for the CP2p2 experiment. Panel (f) same as (b), except for the CP1p1 experiment. Panel (g) same as (b), except for the CPL70 experiment.

We review some key diagnostics for jet speed and explore the inversion structure in more depth in Figure 9. First, Figure 9a shows the average maximum wind speed between the surface and the surface + 100 hPa. All models capture the broad diurnal cycle of the jet, but there are systematic differences in the wind speeds across resolutions, with higher resolutions producing stronger wind speeds (~30% stronger in CP1p1 vs. GLM at night). This systematic difference leads to higher resolution models performing better during the day, but end up being too strong during the night. When considering days with a strong jet by applying a similar criterion to Munday et al. (2022), we reveal considerable differences between the GLM and the high resolution 1.1 km runs (Figure 9b). Nearly all days in the trial meet the strong jet criteria in the 1.1 km simulation at 03Z, whereas this only occurs for 7 days in the GLM. All models produce a jet that is too weak during the early evening, as also found across reanalysis products such as ERA5 (Munday, Engelstaedter, et al., 2023) Note that the GLM here still outperforms ERA5 reanalysis.

Figures 9c and 9d show the surface to surface + 20 hPa minimum temperature, and surface + 20 hPa–surface + 150 hPa maximum temperature respectively, as used in the elevated inversion diagnostic. This allows us to
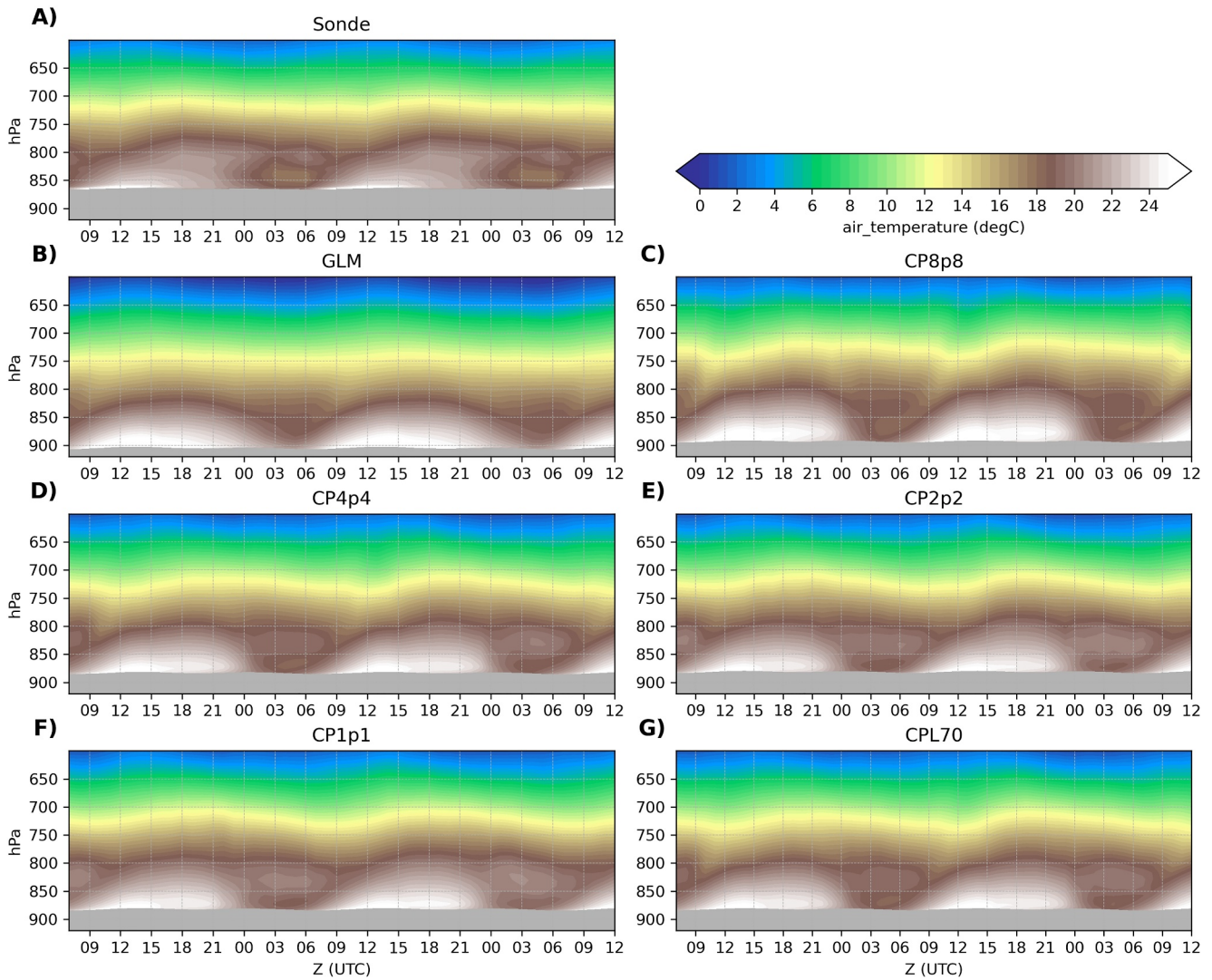
Figure 7. Hovmoeller of air temperature at Marsabit. (a) 3 hourly sonde launches are averaged over the full trial period to produce a hovmoeller of air temperature as a function of time of day. The hovmoeller is shifted and tiled to start at 07UTC, and repeat every 24 hr for subsequent comparison with model data. Pressure levels that fall below the sonde launch pressure are masked in gray. (b) Wind speed in the global model (GLM) experiment as a function of lead time, matching the diurnal cycle (T + 1 hr is 07UTC), averaged across the trial period. Model data is linearly interpolated from the sonde launch site, shifted by 0.02° west and north. Panel (c) same as (b), except for the CP8p8 experiment. Panel (d) same as (b), except for the CP4p4 experiment. Panel (e) same as (b), except for the CP2p2 experiment. Panel (f) same as (b), except for the CP1p1 experiment. Panel (g) same as (b), except for the CPL70 experiment.

understand the relative contribution to inversion strength; that is, whether the lower atmosphere is cooling quickly, or heating aloft (or a combination of both). All models are too warm throughout the day, as found in Figure 7, but the difference between CP models and sonde reduces considerably overnight (Figure 9c). Interestingly, the GLM with convective parametrization has a much warmer surface throughout the day. This may be due to different treatment of cloud in the GA7.1 GLM (which uses the PC2 cloud scheme; Wilson et al., 2008), with knock-on impacts on the radiative balance. The regional model runs all follow a very similar temperature evolution during the night despite their differences in resolution. Examining temperatures in the elevated layer above Marsabit in Figure 9d shows a much larger divergence in model simulations during the day; a warmer layer in the coarse 8.8 km and global simulations as found in Figure 7 relative to the higher resolution models and sonde. All elevated temperatures are too warm in the model during the day compared to the sonde. At night, the cooling of the elevated layer is smallest in the highest resolution run, and closely follows that of the sonde. When considering the combination of these layers and inversion strength in Figure 9e, we find that while all models underestimate the strength of the inversion at Marsabit, the 1.1 km simulation follows that mostly closely of the
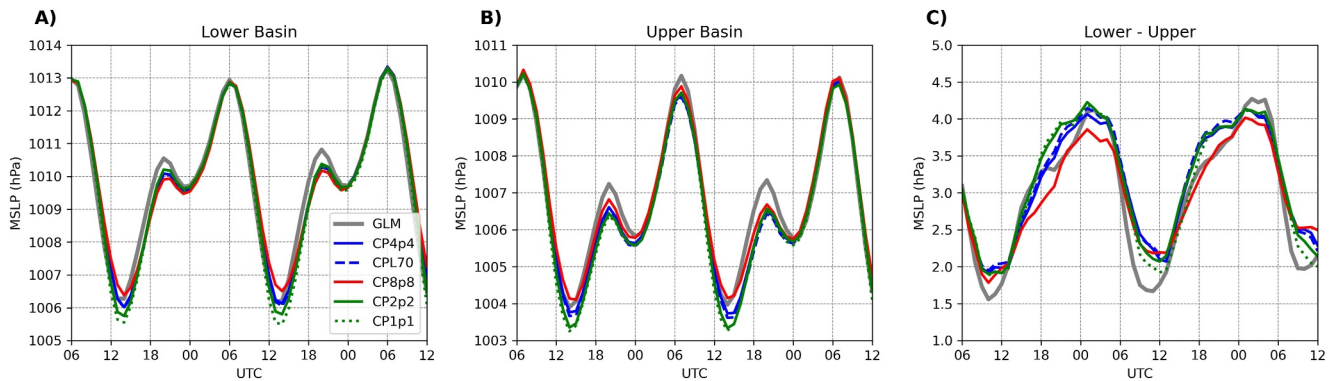
Figure 8. Large scale pressure gradient across the channel. (a) Mean sea level pressure averaged in the pressure gradient force (PGF) box in Figure 1, within the entrance region of the Turkana Jet as a function of model lead-time (mapped onto valid time), averaged over the trial. Panel (b) same as (a), except for the Turkana exit region as defined by PGF box in Figure 1. (c) Average difference between upper and lower basin mean sea level pressure as a function of lead-time.

sonde. We notice two maxima in the tendency of the inversion in the coarser parameterized models; both in the early evening and during the early morning hours. The first peak appears to be due to elevated temperatures staying warmer for longer than observed after sunset (Figure 9d). The second peak is due to the sudden cooling of the elevated layer at 21-00Z in the models (Figure 9d), followed by a stabilization as the jet forms (Figure 9b). Only at resolutions at or less than 2.2 km do we not see the double peak structure so clearly, which compares better to the sonde evolution. Finally, considering days where elevated temperatures exceed surface temperatures, we find a much closer fit at resolutions at or below 2.2 km to the sonde. This appears to be a function of model resolution across the CP simulations, with a stronger late evening peak in the 8.8 km model runs. Note that the mean state of the GLM fails to produce any inversion at any time of day (Figure 9e), and seldom produces one at night during the trial (Figure 9f).

We next consider the link between the jet strength and inversion more closely and investigate daily variability in this relationship during the trial in Figure 10. When considering all hours and days of the trial period, we find that there is a correlation of 0.49 between the strength of the inversion and jet within the sonde observations, corresponding to 25% of jet variability explained by variability in the elevated inversion, consistent with that found in Munday, Engelstaedter, et al. (2023). This correlation is similar to that found in the 2.2 and 1.1 km more simulations, with the coarser models showing a weaker relationship. The GLM is not shown due to its simulation of very few inversions, and so a correlation is not useful. While the trial length is fairly short (29 days), we compare the 00Z jet maximums in the model simulations with the sonde, to determine how good each model is at simulating the jet at T + 18 hr (Figure 10, lower panels). We find the highest resolution model provides the best prediction of jet intensity ($r = 0.8$), and this appears to scale broadly with model resolution. Figures 10g–10l indicate the jet is predictable, despite considerable daily variability. These results suggest that jet strength is predominantly controlled by the representation of local processes, which have been shown to vary considerably across model resolutions, given the models have a similar pressure gradient across the channel (Figure 8) and inherit the same initial and lateral boundary conditions.

4. Conclusions

In this study we have examined the impact of model resolution on simulating the Turkana Jet. along with both local processes and large scale processes tied to it. We intersect these model experiments with the RIFTJet campaign (Munday et al., 2022), providing a novel opportunity to explore model fidelity with in situ observations.

First, we find that the horizontal resolution has a significant bearing on the strength of the Turkana Jet. This leads to increased moisture transport through the channel, along with stronger vertical motion around orography. Interestingly, the number of vertical levels has little bearing on jet strength. We do find that the vertical level-set affects the inversion structure around Marsabit, but not Marsabit itself. When verified against the sonde releases, we find that the simulated jet extends too far in the vertical during the late evening, with wind speeds larger than observed, in model resolutions above 8.8 km. While this may lead to overestimations of water vapor transport through the transect, we note in Figure 5 there is considerable variability in atmospheric structure around Marsabit
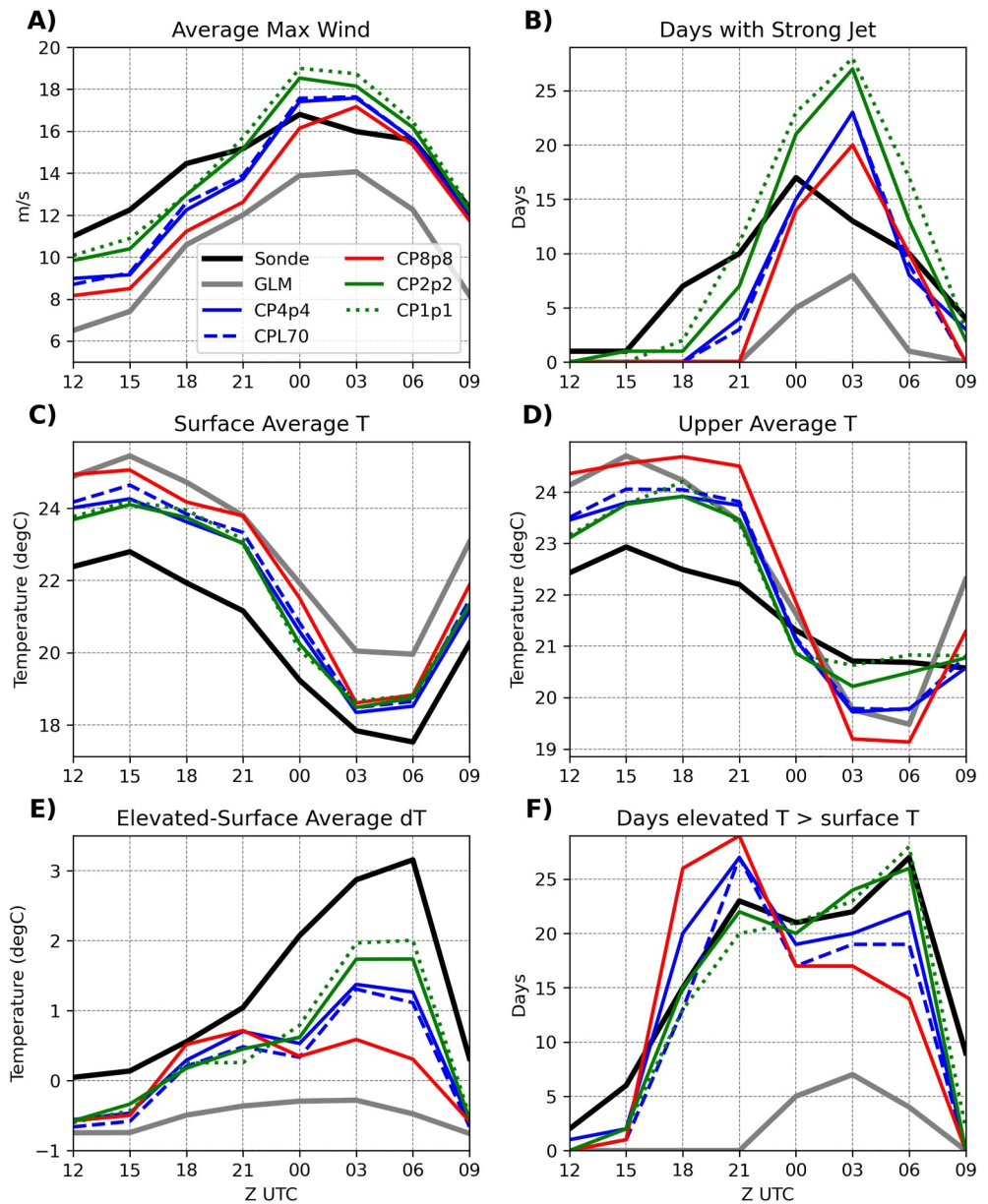
Figure 9. Jet and inversion diagnostics through the diurnal cycle. (a) For both models and the sonde at Marsabit, maximum wind speed between the surface and surface + 100 hPa is calculated, and averaged across the trial. The model T + 18–T + 42 hr forecasts are used. (b) Using the same location/times as in (a), the number of days where the jet exceeds 16 m/s between the surface and surface + 100 hPa, and is at least 4 m/s weaker in the 75 hPa layer above this (surface + 100 hPa to surface + 175 hPa). (c) Using the same location/times as in (a), minimum temperature is computed between the surface and the surface + 20 hPa, and averaged across the trial. (d) Using the same location/times as in (a), the maximum temperature between the surface + 20 hPa and the surface + 150 hPa is computed and averaged across the trial. (e) For each day, computing the difference between maximum elevated temperature (defined in d) and minimum surface temperature (defined in c), and averaging across the trial. (f) As in (e), except calculating the number of days where elevated temperature exceeds surface temperature.

and thus the radiosonde data might not be representative of the broader area. This only occurs at night, whereas the daytime jet is better represented by higher resolution. The elevated inversion structure is substantially improved with increasing horizontal grid resolution.

We also find that models with a higher resolution indicate a stronger relationship between the jet and the strength of the elevated (subsidence) inversion. At resolutions higher than 2.2 km, the link between inversion strength and
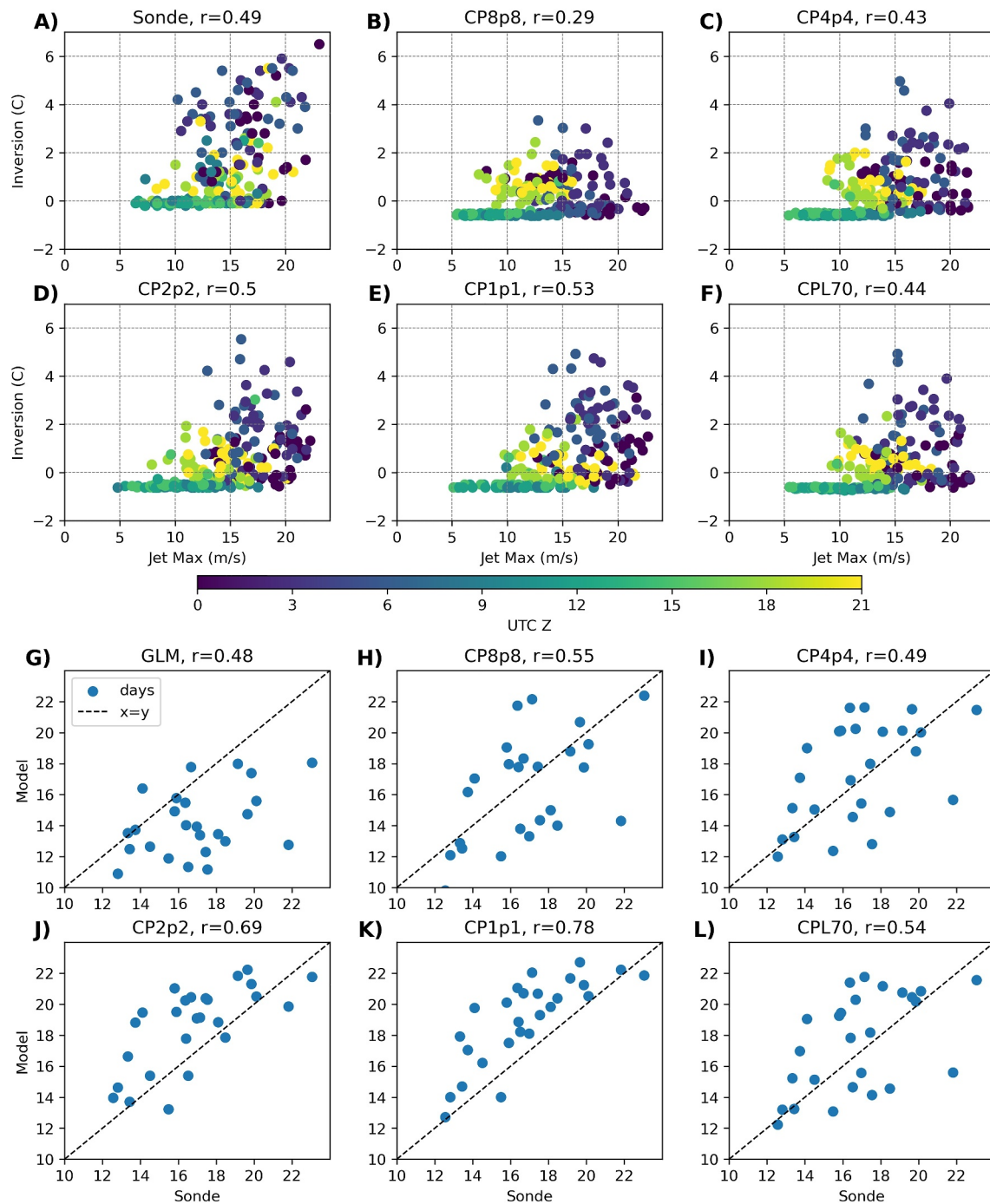
Figure 10. Link between inversion and jet strength, along with jet strength verification. (a) For each sonde launch, the inversion strength and jet maximum are plotted and colored depending on the time of day. Panels (b–f) same as (a), except for the CP8p8, CP4p4, CP2p2, CP1p1, and CPL70 experiments respectively. (g) For each day, 00Z sonde jet maximums, defined as the maximum wind from the surface to surface + 100 hPa, are paired with the global model (GLM) model T + 18 hr forecast. The 1–1 mapping line is overlayed, and the Pearsons correlation coefficient is shown in the title. Panels (h–l) same as (g), except for the CP8p8, CP4p4, CP2p2, CP1p1, and CPL70 experiments respectively.

jet is too strong when compared against the relationship using sonde data. We find that daily jet maxima is predictable, and is better predicted at 1.1 km resolution with a strong correlation of 0.78, despite similar large-scale forcing and pressure gradient across the channel. Considerable variability in daily jet maximum across resolutions suggests improvements at higher resolutions are not due to simply systematically increases the jet

speed, but through improved representation of the jet and related local processes such as its interaction with orography, and elevated inversions. While we cannot deduce causality as these processes are intimately coupled, we demonstrate the importance of being able to represent these at resolutions of 4.4 km and below.

Our results emphasize the need to properly simulate local-scale processes at high resolution and that coarse, parameterized models are likely to produce poor simulations of the jet, and contribute to large downstream biases in regional moisture budgets. A future avenue to build on these results would be to produce a full energy diagnosis of turbulent energy exchange and fluxes to try and better determine causality between the inversion structure and the jet strength. Our recommendation is that 4.4 km is the coarsest model resolution that allows us to represent the main features of the jet and related elevated inversion, but note considerable improvements at finer resolution. These results suggest that much coarser models contributing to climate model intercomparisons will substantially underestimate the jet, and thus be a potential source of error in regional moisture budgets. Further development of scale-aware parameterizations will help. We also advocate for further research in looking at the role of increased model resolution/physics on the large-scale, and how this may affect the pressure gradient across the channel. Here, all models are driven by the same parameterized model, whereas tropical wide model configurations at CP resolution may help us understand the interaction of local and large-scale processes better.

Data Availability Statement

Data derived from the model and sonde data is available in Warner (2023). The ERA5 reanalysis (Hersbach et al., 2020) data set is available publicly at https://cds.climate.copernicus.eu/cdsapp#!/dataset/reanalysis-era5-complete?tab=overview. GPM IMERG data is available publicly at https://gpm.nasa.gov/data/imerg, citable as Huffman et al. (2015).

References

Acosta, R. P., & Huber, M. (2017). The neglected Indo-Gangetic Plains low-level jet and its importance for moisture transport and precipitation during the peak summer monsoon. *Geophysical Research Letters*, *44*(16), 8601–8610. https://doi.org/10.1002/2017gl074440

Almazroui, M., Saeed, F., Saeed, S., Nazrul Islam, M., Ismail, M., Klutse, N. A. B., & Siddiqui, M. H. (2020). Projected change in temperature and precipitation over Africa from CMIP6. *Earth Systems and Environment*, *4*(3), 455–475. https://doi.org/10.1007/s41748-020-00161-x

Best, M. J., Pryor, M., Clark, D. B., Rooney, G. G., Essery, R., Ménard, C. B., et al. (2011). The Joint UK Land Environment Simulator (JULES), model description–Part 1: Energy and water fluxes. *Geoscientific Model Development*, *4*(3), 677–699. https://doi.org/10.5194/gmd-4-677-2011

Blackadar, A. K. (1957). Boundary layer wind maxima and their significance for the growth of nocturnal inversions. *Bulletin of the American Meteorological Society*, *38*(5), 283–290. https://doi.org/10.1175/1520-0477-38.5.283

Bloomfield, H. C., Wainwright, C. M., & Mitchell, N. (2022). Characterizing the variability and meteorological drivers of wind power and solar power generation over Africa. *Meteorological Applications*, *29*(5), e2093. https://doi.org/10.1002/met.2093

Bush, M., Boutle, I., Edwards, J., Finnenkoetter, A., Franklin, C., Hanley, K., et al. (2023). The second met office unified model/JULES regional atmosphere and land configuration, RAL2. *Geoscientific Model Development Discussions*, *16*(6), 1–35. https://doi.org/10.5194/gmd-16-1713-2023

Cullen, M. J. P. (1993). The unified forecast/climate model. *The Meteorological Magazine*, *122*(1449), 81–94.

Dieminger, W., Hartmann, G. K., & Leitinger, R. (1996). Atmospheric tides. *The Upper Atmosphere: Data Analysis and Interpretation*, 97–109. https://doi.org/10.1007/978-3-642-78717-1_3

Donlon, C. J., Martin, M., Stark, J., Roberts-Jones, J., Fiedler, E., & Wimmer, W. (2012). The operational sea surface temperature and sea ice analysis (OSTIA) system. *Remote Sensing of Environment*, *116*, 140–158. https://doi.org/10.1016/j.rse.2010.10.017

Farr, T. G., Rosen, P. A., Caro, E., Crippen, R., Duren, R., Hensley, S., et al. (2007). The shuttle radar topography mission. *Reviews of Geophysics*, *45*(2), RG2004. https://doi.org/10.1029/2005rg000183

Finney, D. L., Marsham, J. H., Jackson, L. S., Kendon, E. J., Rowell, D. P., Boorman, P. M., et al. (2019). Implications of improved representation of convection for the East Africa water budget using a convection-permitting model. *Journal of Climate*, *32*(7), 2109–2129. https://doi.org/10.1175/jcli-d-18-0387.1

Giuliani, M., Zaniolo, M., Sinclair, S., Micotti, M., Van Orshoven, J., Burlando, P., & Castelletti, A. (2022). Participatory design of robust and sustainable development pathways in the Omo-Turkana river basin. *Journal of Hydrology: Regional Studies*, *41*, 101116. https://doi.org/10.1016/j.ejrh.2022.101116

Hafner, M., Tagliapietra, S., de Strasser, L., Hafner, M., Tagliapietra, S., & de Strasser, L. (2018). Prospects for renewable energy in Africa. *Energy in Africa: Challenges and Opportunities*, 47–75. https://doi.org/10.1007/978-3-319-92219-5_3

Hamilton, H. L., Núñez Ocasio, K. M., Evans, J. L., Young, G. S., & Fuentes, J. D. (2020). Topographic influence on the African easterly jet and African easterly wave energetics. *Journal of Geophysical Research: Atmospheres*, *125*(8), e2019JD032138. https://doi.org/10.1029/2019jd032138

Hartman, A. T. (2018). An analysis of the effects of temperatures and circulations on the strength of the low-level jet in the Turkana Channel in East Africa. *Theoretical and Applied Climatology*, *132*(3–4), 1003–1017. https://doi.org/10.1007/s00704-017-2121-x

Helfand, H. M., & Schubert, S. D. (1995). Climatology of the simulated Great Plains low-level jet and its contribution to the continental moisture budget of the United States. *Journal of Climate*, *8*(4), 784–806. https://doi.org/10.1175/1520-0442(1995)008<0784:cotsgp>2.0.co;2

Hersbach, H., Bell, B., Berrisford, P., Hirahara, S., Horányi, A., Muñoz-Sabater, J., et al. (2020). The ERA5 global reanalysis. *Quarterly Journal of the Royal Meteorological Society*, *146*(730), 1999–2049. https://doi.org/10.1002/qj.3803

Hou, A. Y., Kakar, R. K., Neeck, S., Azarbarzin, A. A., Kummerow, C. D., Kojima, M., et al. (2014). The global precipitation measurement mission. *Bulletin of the American Meteorological 459 Society*, *95*(5), 701–722. https://doi.org/10.1175/bams-d-13-00164.1

Huffman, G. J., Bolvin, D. T., Braithwaite, D., Hsu, K., Joyce, R., Xie, P., & Yoo, S. H. (2015). NASA global precipitation measurement (GPM) integrated multi-satellite retrievals for GPM (IMERG). *Algorithm Theoretical Basis Document (ATBD) Version*, *4*(26), 30.

Indeje, M., Semazzi, F. H., Xie, L., & Ogallo, L. J. (2001). Mechanistic model simulations of the East African climate using NCAR regional climate model: Influence of large-scale orography on the Turkana low-level jet. *Journal of Climate*, *14*(12), 2710–2724. https://doi.org/10.1175/1520-0442(2001)014<2710:mmsote>2.0.co;2

King, J. A., Engelstaedter, S., Washington, R., & Munday, C. (2021). Variability of the Turkana low-level jet in reanalysis and models: Implications for rainfall. *Journal of Geophysical Research: Atmospheres*, *126*(10), e2020JD034154. https://doi.org/10.1029/2020jd034154

Kinuthia, J. H. (1992). Horizontal and vertical structure of the Lake Turkana jet. *Journal of Applied Meteorology and Climatology*, *31*(11), 1248–1274. https://doi.org/10.1175/1520-0450(1992)031<1248:havsot>2.0.co;2

Kinuthia, J. H., & Asnani, G. C. (1982). A newly found jet in North Kenya (Turkana Channel). *Monthly Weather Review*, *110*(11), 1722–1728. https://doi.org/10.1175/1520-0493(1982)110<1722:anfjin>2.0.co;2

Kirshbaum, D. J. (2020). Numerical simulations of orographic convection across multiple gray zones. *Journal of the Atmospheric Sciences*, *77*(10), 3301–3320. https://doi.org/10.1175/jas-d-20-0035.1

Laroche, S., & Sarrazin, R. (2013). Impact of radiosonde balloon drift on numerical weather prediction and verification. *Weather and Forecasting*, *28*(3), 772–782. https://doi.org/10.1175/waf-d-12-00114.1

Mathon, V., Laurent, H., & Lebel, T. (2002). Mesoscale convective system rainfall in the Sahel. *Journal of Applied Meteorology and Climatology*, *41*(11), 1081–1092. https://doi.org/10.1175/1520-0450(2002)041<1081:mcsrit>2.0.co;2

Misiani, H. O., Finney, D. L., Segele, Z. T., Marsham, J. H., Tadege, A., Artan, G., & Atheru, Z. (2020). Circulation patterns associated with current and future rainfall over Ethiopia and South Sudan from a convection-permitting model. *Atmosphere*, *11*(12), 1352. https://doi.org/10.3390/atmos11121352

Montini, T. L., Jones, C., & Carvalho, L. M. (2019). The South American low-level jet: A new climatology, variability, and changes. *Journal of Geophysical Research: Atmospheres*, *124*(3), 1200–1218. https://doi.org/10.1029/2018jd029634

Munday, C., Engelstaedter, S., Ouma, G., Ogutu, G., Olago, D., Ong'ech, D., et al. (2022). Observations of the Turkana jet and the East African dry tropics: The RIFTJet field campaign. *Bulletin of the American Meteorological Society*, *103*(8), E1828–E1842. https://doi.org/10.1175/bams-d-21-0214.1

Munday, C., Engelstaedter, S., Washington, R., Ogutu, G., Olago, D., Ouma, G., et al. (2023). The Turkana Jet diurnal cycle in observations and reanalysis. *Journal of Climate*. https://doi.org/10.1175/jcli-d-23-0325.1

Munday, C., Savage, N., Jones, R. G., & Washington, R. (2023). Valley formation aridifies East Africa and elevates Congo Basin rainfall. *Nature*, *615*(7951), 276–279. https://doi.org/10.1038/s41586-022-05662-5

Munday, C., Washington, R., & Hart, N. (2021). African low-level jets and their importance for water vapor transport and rainfall. *Geophysical Research Letters*, *48*(1), e2020GL090999. https://doi.org/10.1029/2020gl090999

Nicholson, S. (2016). The Turkana low-level jet: Mean climatology and association with regional aridity. *International Journal of Climatology*, *36*(6), 2598–2614. https://doi.org/10.1002/joc.4515

Nicholson, S. E. (2017). Climate and climatic variability of rainfall over eastern Africa. *Reviews of Geophysics*, *55*(3), 590–635. https://doi.org/10.1002/2016rg000544

Oscar, L., Nzau, M. J., Ellen, D., Franklin, O., Rachel, J., Richard, W., & Tom, W. (2022). Characteristics of the Turkana low-level jet stream and the associated rainfall in CMIP6 models. *Climate Dynamics*, 1–17. https://doi.org/10.1007/s00382-022-06499-4

Shaw, J. (2018). Numerical representation of mountains in atmospheric models PhD Thesis. Department of Meteorology, University of Reading. Retrieved from https://centaur.reading.ac.uk/82281/

Sheridan, P., Xu, A. L., Li, J., & Furtado, K. (2023). Use of targeted orographic smoothing in very high resolution simulations of a downslope windstorm and rotor in a sub-tropical highland location. *Advances in Atmospheric Sciences*, *40*(11), 2043–2062. https://doi.org/10.1007/s00376-023-2298-0

Smith, R. N. B. (1990). A scheme for predicting layer clouds and their water content in a general circulation model. *Quarterly Journal of the Royal Meteorological Society*, *116*(492), 435–460. https://doi.org/10.1002/qj.49711649210

Spavins-Hicks, Z. D., Washington, R., & Munday, C. (2021). The Limpopo low-level jet: Mean climatology and role in water vapor transport. *Journal of Geophysical Research: Atmospheres*, *126*(16), e2020JD034364. https://doi.org/10.1029/2020jd034364

Stratton, R. A., Senior, C. A., Vosper, S. B., Folwell, S. S., Boutle, I. A., Earnshaw, P. D., et al. (2018). A Pan-African convection-permitting regional climate simulation with the met office unified model: CP4-Africa. *Journal of Climate*, *31*(9), 3485–3508. https://doi.org/10.1175/jcli-d-17-0503.1

Vizy, E. K., & Cook, K. H. (2019). Observed relationship between the Turkana low-level jet and boreal summer convection. *Climate Dynamics*, *53*(7–8), 4037–4058. https://doi.org/10.1007/s00382-019-04769-2

Walters, D., Baran, A. J., Boutle, I., Brooks, M., Earnshaw, P., Edwards, J., et al. (2019). The Met Office Unified Model global atmosphere 7.0/7.1 and JULES global land 7.0 configurations. *Geoscientific Model Development*, *12*(5), 1909–1963. https://doi.org/10.5194/gmd-12-1909-2019

Warner, J. L. (2023). Data used to generate figures within the manuscript 2023JD040299 [Dataset]. https://doi.org/10.5281/zenodo.10033773

Warner, J. L., Petch, J., Short, C. J., & Bain, C. (2023). Assessing the impact of an NWP warm-start system on model spin-up over tropical Africa. *Quarterly Journal of the Royal Meteorological Society*, *149*(751), 621–636. https://doi.org/10.1002/qj.4429

Wilson, D. R., & Ballard, S. P. (1999). A microphysically based precipitation scheme for the UK Meteorological Office Unified Model. *Quarterly Journal of the Royal Meteorological Society*, *125*(557), 1607–1636. https://doi.org/10.1256/smsqj.55706

Wilson, D. R., Bushell, A. C., Kerr-Munslow, A. M., Price, J. D., & Morcrette, C. J. (2008). PC2: A prognostic cloud fraction and condensation scheme. I: Scheme description. *Quarterly Journal of the Royal Meteorological Society: A Journal of the Atmospheric Sciences, Applied Meteorology and Physical Oceanography*, *134*(637), 2093–2107. https://doi.org/10.1002/qj.333

Zhao, S., & Cook, K. H. (2021). Influence of Walker circulations on East African rainfall. *Climate Dynamics*, *56*(7–8), 2127–2147. https://doi.org/10.1007/s00382-020-05579-7

Erratum

The originally published version of this article omitted a funding source from the Acknowledgments. The Acknowledgments should read as follows: "This work and its contributors (James Warner) were funded by the Met Office Weather and Climate Science for Service Partnership (WCSSP) South Africa project, which is supported by the Department for Science, Innovation & Technology (DSIT). The RIFTJet project and data are part of the REACH water security program funded by the FCDO. However, the views expressed, and information contained in it, are not necessarily those of or endorsed by the FCDO, which can accept no responsibility for such views or information or for any reliance placed on them." The errors have been corrected, and this may be considered the authoritative version of record.